Faraday-rotation self-interference method for electron beam duration measurement in the laser wakefield accelerator

Jiaqi Liu(刘佳琦)[1,2], Wentao Li(李文涛)[1,3*], Jiansheng Liu(刘建胜)[1,4], Zhiyong Qin(秦志勇)[1,2], Wentao Wang(王文涛)[1], Rong Qi(齐 荣)[1], Zhijun Zhang(张志钧)[1], Changhai Yu(余昌海)[1], Ming Fang(方 明)[1,2], Cheng Wang(王成)[1], and Ruxin Li(李儒新)[1,4,5***]**

[1]Shanghai Institute of Optics and Fine Mechanics, Chinese Academy of Sciences, Shanghai 201800, China

[2]University of Chinese Academy of Sciences, Beijing 100049, China

[3]Department of Physics, SUPA and University of Strathclyde, Glasgow G4 0NG, United Kingdom

[4]IFSA Collaborative Innovation Center, Shanghai Jiao Tong University, Shanghai 200240, China

[5]School of Physical Science and Technology, ShanghaiTech University, Shanghai 200031, China

Corresponding author: wentao.li@strath.ac.uk; ** corresponding author: michaeljs_liu@siom.ac.cn; * corresponding author: ruxinli@mail.siom.ac.cn*

Abstract

A real-time single-shot measurement of the femtosecond electron beam duration in the laser wakefield accelerators was discussed for both experimental design and theoretical analysis, which combines the magnetic field based polarimetry and optical interferometry. The probe pulse polarization is rotated by the azimuthal magnetic field of the electron beam and then introduced into a Michelson-type interferometer for self-interference. The electron beam duration is obtained from the region size of the interference fringes, which is independent of the pulse width of the probe laser. Using a larger magnification system or incident angle, the measurement resolution can be less than $1\ fs$.

1. Introduction

Great improvements have been achieved in laser wakefield accelerators (LWFAs) in the past few years.[1, 2] Stable quasi-monoenergetic electron beams from LWFA are available using the steady laser equipment and gas cell.[3, 4] Electron beams with GeV energy have also been demonstrated with self-injection[4, 5], ionization injection[6, 7] and cascaded LWFA[8]. These progresses paved the road towards the applications such as radiation source[9] and ultra-fast imaging. The precise and complete diagnostics for the electron beams are necessary before extending these applications. However, among all the parameters, some can be measured by the traditional methods, such as the energy spectrum and beam charge; others are completely beyond these methods' abilities. For instance, measurement of the electron beam duration is important for its application in obtaining ultrashort and high brilliant X-ray source. According to the particle-in-cell (PIC) simulation results,[10] the electron beam duration is inherently shorter than the plasma wave length, which is typically in a range of $10-30\ \mu m$ for plasma density of $10^{18}\ cm^{-3}$. The electron beam duration is usually shorter than 10 fs, which is too short to be measured by the traditional techniques.

Coherent transition radiation (CTR) in THz spectral region, which is emitted when the electron beam transmits through a metal foil, has been used as a single-shot measurement of the electron beam duration longer than $30\ fs$.[11] The near- to mid-

infrared CTR spectroscopy has also been reported to be used to measure the electron beam with durations of a few femtoseconds,[12] but it can not obtain the beam shape in the single-shot mode and has a limited detecting range. Electron oscillation of its energy distribution caused by the laser field was also used to measure its duration,[13] but the electron beam quality would be affected during the measurement. Real-time measurement of beam duration by magnetic field of the accelerated electron beam inside the wake has also been demonstrated.[14] However, the length of the polarization-rotated probe laser τ_{rot} is the convolution of the beam duration τ_{beam}, transit time (time for the probe laser transmits the azimuthal magnetic field region) τ_{trans}, imaging resolution τ_{res} and probe laser duration τ_{pro}, which add quadratically. Among all these parameters, τ_{pro} will sufficiently enlarge the result because it's much longer than τ_{beam}. Additionally, τ_{pro} is sensitive to the group-velocity dispersion[15], which also introduces inaccuracy in the beam duration. Therefore, a probe laser within $10\,fs$ is required in this scheme. Such a short pulse is difficult to obtain with current facilities and additional synchronization equipment is required.

In this letter, we present a Faraday-rotation self-interference (FRSI) method for the measurement of an electron beam with duration of femtosecond. This method is a combination of the Faraday-rotation effect[16] and the Michelson-type interferometry. The polarization of the probe laser is rotated by the azimuthal magnetic field of the electron beam, just as the reference [14] descripted. The difference is that the Glan-laser polarizer only allows the transmission of the polarization-rotated light. And the transmitted light is incident into a Michelson-type interferometer for self-interference after a magnification system. Because the region size of the interference fringes is only related to the magnetic field region of the electron beam, it is independent of τ_{pro}. By adjusting the magnification and the angle between the interfering light beam, the electron beam duration resolution of FRSI can be improved as short as $1\,fs$.

2. Operation of the Faraday-rotation self-interference (FRSI) method

FRSI is based on two well-known techniques, the Faraday-rotation effect caused by the azimuthal magnetic field of the electron beam, and the Michelson-type interferometer. The first mode of the experimental set-ups that using the Faraday-rotation effect is similar to the scheme in reference[14] as shown in Fig. 1. The probe light beam is split from the driving pulse, which propagates perpendicularly to the driver and accelerated electron beam. A delay line can be used to adjust the synchronization between the probe light and driving laser. Because the electron beam in LWFAs has a high energy, charge (~100 pC) and ultrashort duration (~10 fs), the generated current can be as high as ~10 kA, which leads to a surrounding strong azimuthal magnetic field. The azimuthal magnetic field is several orders of magnitude higher than that generated by the displacement current in the bubble, which is homogenous in the longitudinal direction. The strong magnetic field of the electron beam will change the polarization of the transverse incident probe laser passing above or below the electron beam inversely because of the Faraday-rotation effect. The angle of the probe laser polarization rotated by the azimuthal magnetic field $\vec{B}_{\varphi}$ is calculated by

$$\varphi_{rot} = \frac{e}{2m_e c n_{cr}} \int_l n_e \vec{B}_{\varphi} \cdot d\vec{s}, \tag{1}$$

where m_e, e and c are the electron mass, electron charge and light speed in vacuum. $n_{cr} \approx 1.72 \times 10^{21}\, cm^{-3}$ is the critical density for the probe pulse of a $0.8\,\mu m$ wavelength, and n_e is the electron density. $d\vec{s}$ is the path element along the propagation path l of the probe pulse through the plasma region.

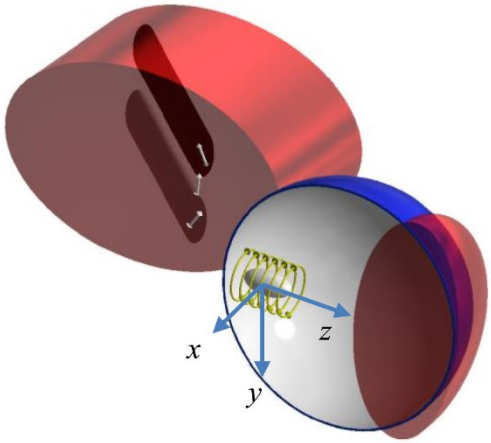

Figure 1. Layout of the polarization-rotated light by the azimuthal magnetic field, which is generated by the accelerated electron beam. The polarizations of the light passing above and below the beam are rotated oppositely.

A Glan-laser polarizer with a 90-degree angle away from the initial probe pulse polarization is located before the entrance of interferometer. The extinction ratio of the Glan-laser polarizer is $10^5{:}1$ so that it only allows the transmission of the light with polarization rotated by the magnetic field, as two dark regions in cylinder shape in Fig. 1. Because the velocity of the electron beam is almost identical to the light speed, the dark region is oblique. The angle between the axis of the cylinder and the propagation direction of the probe light is 45^o. Before entering the Michelson-type interferometer, the polarization-rotated region of the probe light is magnified by a pair of lens.

In the Michelson-type interferometer, the incident probe light is split into two beams (L1 and L2) by a 50:50 beamsplitter. L1 is reflected and flipped horizontally by a mirror, as shown in Fig. 2. L2 is reflected by a right-angle prism for two times. The orientation angle of the regions of L1 and L2 are symmetrical along the Z-axis in the (x, z) plane. A small incident angle θ is introduced between the propagation directions of these two beams by adjusting the mirror. As a result, L1 and L2 interfere with each other in the overlapping region, which is recorded by a CCD camera. Since the region size of the interference fringes only depends on the scale of the magnetic field region, which is not affected by the probe beam duration, the length of the electron beam can be determined from width and height of the interference region with high accuracy.

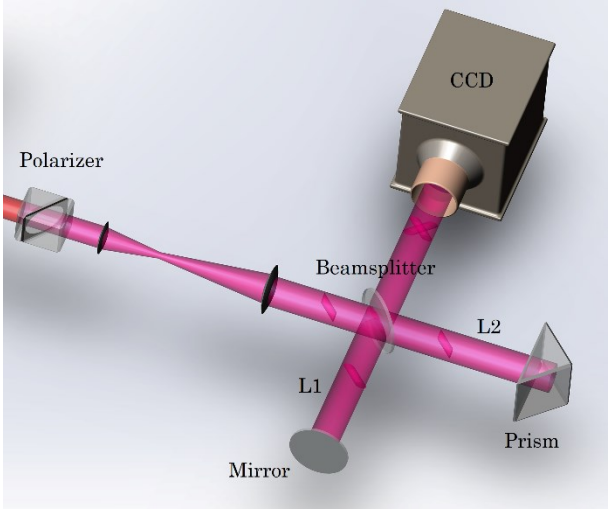

Figure 2. Layout of the Michelson-type interferometer. The polarizer angle is 90-degree angle away from the initial polarization of the probe laser, which only allows the transmission of the polarization-rotated light. The probe beam is amplified N times by a pair of lens and then split into L1 and L2 by a beamsplitter. L1 and L2 interfers with each other and the interference fringes is recorded by a CCD camera.

3. Theoretical analysis of the FRSI method

The distribution of the rotation angle φ_{rot} on the probe pulse can be calculated from the PIC simulation result from Eq. (1). Fig. 3(a) shows a typical magnetic field distribution of the electron beam in the transverse cross-section in the self-injected LWFA simulation results with parameters of $a_0 = 2$ and $n_e = 6 \times 10^{18}\, cm^{-3}$, where the electron beam propagates along the Z-axis. The magnetic field caused by displacement current is negligible compared to that caused by the accelerated electron beam. The rotation angle of the polarization can be calculated by tracking the magnetic field and electron density distribution in the propagation route of the probe light without considering the movement of the electron beam along the Z-axis during the transition process. Fig. 3(b) shows the distribution of the rotation angle φ_{rot} on the probe pulse. As we discussed before, φ_{rot} is mainly introduced by the magnetic field of the electron beam and the contribution from the displacement current in the bubble is rare.

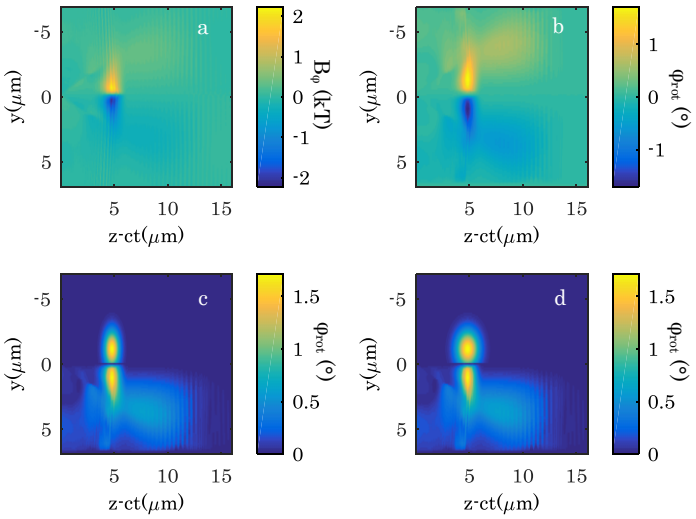

Figure 3. (a) Magnetic field distribution and (b) rotation angle of the polarization calculated by tracking the magnetic field and the electron density in the propagation route of the probe laser using Eq. (1) in the (y, z) plane from PIC simulations. Distribution of the polarization rotation angle considering a Gaussian magnetic field profile (c) without and (d) with considering the transit time of the probe light.

To clarify the relation between the region size of the interference fringes and electron beam duration, the analytical description of the polarization rotation angle distribution is required in our scheme. Since azimuthal magnetic field is rotational symmetrical round the Z-axis, and only the polarization of the light above and below the electron beam can be rotated by the magnetic field, φ_{rot} is inversion symmetry around the Z-axis. Therefore, we only consider the top half of the rotation angle for simplicity. The analytic calculation can be further simplified by assuming that it has the Gaussian intensity profile in the (y, z) plane, where $(0,0)$ is defined as the position with the maximum rotation angle φ_0. The magnetic field region is assumed to have a full width at half maximum (FWHM) of r_{mag} along the Y-axis and a full length at half maximum (FLHM) of L_{mag} along the Z-axis, among which L_{mag} is identical to the FLHM electron beam duration. Without considering the transit time of the probe laser, the distribution of the rotation angle φ_{rot} in the (y, z) plane is formulated as

$$\varphi_{rot}(y,z) = \varphi_0 e^{-4\ln 2\left[\frac{y^2}{r_{mag}^2}+\frac{z^2}{L_{mag}^2}\right]}, \tag{2}$$

The distribution map from Eq. (2) is shown in the top half in Fig. 3(c), which agrees well with the simulation result in the bottom half in Fig. 3(c). Further, if transit time of the probe pulse through the azimuthal magnetic field is considered as $2r_{mag}/c$, the distribution of the rotation angle can then be expressed as

$$\varphi_{rot}(y,z,t) = \varphi_0 e^{-4\ln 2\left[\frac{y^2}{r_{mag}^2}+\frac{(z-ct)^2}{L_{mag}^2+4r_{mag}^2}\right]}. \tag{3}$$

The profile is shown in the top half in Fig. 3(d), which is obviously wider along the Z-axis than the simulation result in the bottom half in Fig. 3(d).

The probe laser pulse propagates along the X-axis with the electric field described as $E(x,t) = E_0 cos(\omega t - kx) e^{-2\ln 2(\frac{x-ct}{ct_{pro}})^2}$. Its wave front overlaps with the electron beam at $t =$

$-\tau_{pro}$ and $x = 0$. When it is travelling through the magnetic field region, its polarization will be rotated by a small angle of $\varphi_{rot}(y,z,t)$ degrees. Using the Glan-laser polarizer, which is a 90-degree angle away from the initial probe pulse polarization as discussed above, the transmitted electric field component is $E(x,t)\varphi_{rot}(y,z,t)$. Combing it with the Eq. (3), the normal component of the electric field becomes

$$E(x,y,z,t) = E_0\varphi_0 cos(\omega t - kx)e^{-2\,ln\,2\left[(\frac{x-ct}{c\tau_{pro}})^2+\frac{2y^2}{r_{mag}^2}+\frac{2(z-ct)^2}{L_{mag}^2+4r_{mag}^2}\right]}. \quad (4)$$

Since the polarization of the probe pulse can only be rotated when it passes through the magnetic field, the time range for Eq. (4) should be limited from $-\tau_{pro}$ to τ_{pro}.

Before the probe light is incident into the Michelson-type interferometer, the probe light is magnified N times by a pair of lens. Additionally, if the propagation length of the electron beam during the probe light is considered, the axial orientation of the transmitted laser in an oblique cylinder shape is 45^o away from the initial propagation direction of the probe light. The electric field of the dark region in Fig. 1 can be expressed as

$$E(x,y,z,t) = E_0\varphi_0 cos(\omega t - kx)e^{-2\,ln\,2\left[(\frac{x-ct}{c\tau_{pro}})^2+\frac{2y^2}{N^2r_{mag}^2}+\frac{2(z+x-ct)^2}{N^2(L_{mag}^2+4r_{mag}^2)}\right]}. \quad (5)$$

The probe beam will be split equally into two beams, which are noted as L1 and L2 in Fig. 2. L1 is reflected by the beamsplitter and mirror for two times, with the inclination angle staying 45^o away from the X-axis in the (x,z) plane. Meanwhile, L2 will be reflected by the right-angle prism and the beamsplitter for three times, and its inclination angle becomes 135^o away from the X-axis. L1 and L2 are symmetrical along the Z-axis. Both L1 and L2 propagate along the Z-axis after the reflection before entering the CCD camera. The electric fields of L1 and L2 become

$$E_1(x,y,z,t) = \frac{1}{2}E_0\varphi_0\, cos(\omega t - kz)\, e^{-2\,ln\,2\left[\left(\frac{z-ct}{c\tau_{pro}}\right)^2+\frac{2y^2}{N^2r_{mag}^2}+\frac{2(z-x-ct)^2}{N^2\left(L_{mag}^2+4r_{mag}^2\right)}\right]}, \quad (6)$$

$$E_2(x,y,z,t) = \frac{1}{2}E_0\varphi_0\, cos(\omega t - kz)\, e^{-2\,ln\,2\left[\left(\frac{z-ct}{c\tau_{pro}}\right)^2+\frac{2y^2}{N^2r_{mag}^2}+\frac{2(z+x-ct)^2}{N^2\left(L_{mag}^2+4r_{mag}^2\right)}\right]}. \quad (7)$$

From Eq. (6) and (7), the individual intensity profile of L1 or L2 recorded by the CCD camera integrated from $-\tau_{pro}$ to τ_{pro} will be affected by both the region size of magnetic field and the probe pulse duration τ_{pro}. A larger region size of the magnetic field can expand its scale in the (x,y) plane. Additionally, τ_{pro} will enhance the intensity region size along the X-axis. The intensity peaks of L1 and L2 overlap with each other at the origin of this new coordinate system at $t = -\tau_{pro}$. By adjusting the position and angle of the right-angle prism, L1 and L2 can be normally incident to the CCD synchronously and these two polarization-rotated region will overlap symmetrically around the Z-axis in the (x,z) plane. However, if a tiny angle θ between L1 and the Z-axis is introduced by adjusting the mirror, the electric field of L1 is modified by

$$E_1(x,y,z,t) \approx \frac{1}{2}E_0\varphi_0 cos[\omega t - k(z + x\theta)]e^{-2\,ln\,2\left[\left(\frac{z-ct}{c\tau_{pro}}\right)^2+\frac{2y^2}{N^2r_{mag}^2}+\frac{2(z-x-ct)^2}{N^2\left(L_{mag}^2+4r_{mag}^2\right)}\right]}. \quad (8)$$

L1 and L2 can interfere with each other in the (x,y) plane, which is recorded by a CCD camera. The intensity profile of the two probe beams can be obtained by substituting equation (7) and (8) into the equation

$$I(x,y,z,t) = |E_1(x,y,z,t) + E_2(x,y,z,t)|^2, \quad (9)$$

and the image recorded by the CCD camera located in plane $z = z'$ can be expressed as

$$I_{CCD}(x,y) = \int_{-\tau_{pro}}^{\tau_{pro}} |E_1(x,y,z,t) + E_2(x,y,z,t)|^2 \delta(z - z')dt. \quad (10)$$

The interference-term in Eq. (10) is

$$I_{12}(x,y) \propto I_{12} \int_{-\tau_{pro}}^{\tau_{pro}} cos(kx\theta) \exp\left\{-4\,ln\,2\left[\frac{(z'-ct)^2}{(c\tau_{pro})^2} + \frac{2y^2}{N^2 r_{mag}^2} + \frac{2x^2+2(z'-ct)^2}{N^2(L_{mag}^2+4r_{mag}^2)}\right]\right\} dt. \quad (11)$$

From Eq. (10) and (11), the image recorded by CCD can be considered as the mixture of a background intensity profile and interference fringes. The scale of the background intensity profile will be expanded for both a larger magnetic field region and longer τ_{pro} as we discussed before. However, as the term $\int_{-\tau_{pro}}^{\tau_{pro}} \exp\left\{-4\,ln\,2\left[\frac{(z'-ct)^2}{(c\tau_{pro})^2} + \frac{2(z'-ct)^2}{N^2(L_{mag}^2+4r_{mag}^2)}\right]\right\} dt$ only modulates the intensity peak of the interference fringes, the region scale of the interference fringes in the (x,y) plane is independent of τ_{pro}. The interference fringes are limited in a range with FWHM sizes of $Nr_{mag}/\sqrt{2}$ in the Y-axis and $N\sqrt{(L_{mag}^2 + 4r_{mag}^2)}/\sqrt{2}$ in the X-axis. The fringe interval along the X-axis is only determined by θ. τ_{pro} only affects the intensity of the interference fringes. Therefore, by measuring the height and the width of the interference region, the duration of the electron beam L_{mag} could be determined.

4. Measurement of the electron beam duration with the FRSI method

The magnetic field region radius and electron beam duration can be determined from the region size of the interference fringes, which is recorded by the CCD camera. Here we offer a theoretical example when the probe beam has a duration of $100\,fs$ and magnetic field has a duration and radius of $5\,fs$ and $2\,\mu m$ for explanation. The beam waist of the polarization-rotated light is magnified 10 times by the magnification system before the Glan-laser polarizer. And the angle θ between L1 and L2 is assumed to be 5^o. The pixel size of the CCD camera is assumed to be $5\,\mu m$, considering the magnification ratio, the spatial resolution of the intensity profile is $0.5\,\mu m$. Fig. 4(a) shows the intensity distribution I_2 of the single beam L2 on the camera imaging plane, which is calculated from Eq. (7). Fig. 4(b) shows the intensity profile I_{CCD} in the overlapping region of L1 and L2 from Eq. (10), which contains the interference fringes. Fig. 4(c) and (d) plot the normalized intensity traces integral along the Y-axis and X-axis of the intensity profile in Fig. 4(a), respectively. Fig. 4(e) shows the normalized intensity trace integral along the Y-axis of the intensity profile in Fig. 4(b). The individual interference fringes I_{12} is retrieved by $I_{12} = I_{CCD} - 2I_2$, and the normalized intensity trace integral along the Y-axis is plotted in Fig. 4(f). The scale of the interference fringes are calculated from the intensity envelopes in Fig. 4(c) and (f), whose FWHM are $14.5\,\mu m$ and $31.5\,\mu m$, respectively. According to the analysis above, the radius r_{mag} and duration L_{mag} of the magnetic field can be determined to be $2.05\,\mu m$ and $1.74\,\mu m$ ($5.8fs$), which are quite consistent with the preset values.

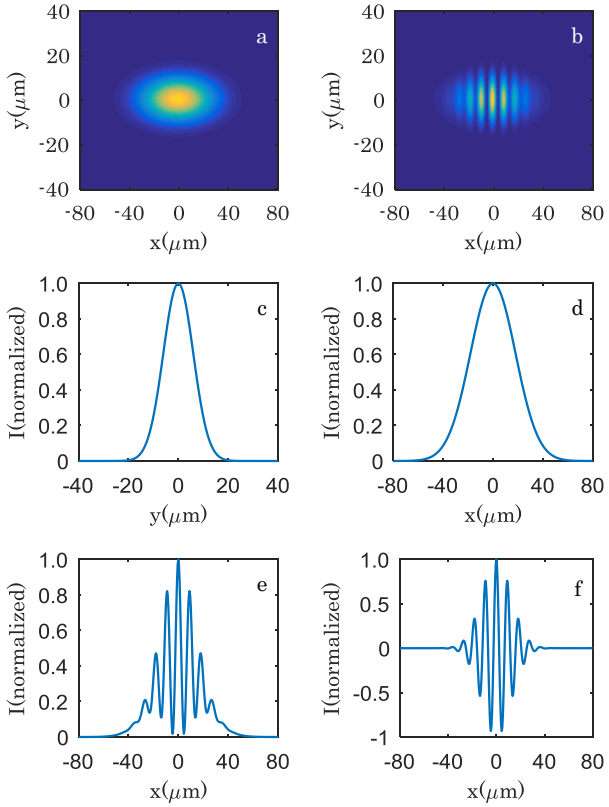

Figure 4. Intensity distributions of (a) L2 from Eq. (7) and (b) the interference fringes of L1 and L2 from Eq. (10) on the CCD imaging plane with $\tau_{pro} = 100fs$. Normalized intensity traces of the intensity distribution of L2 integral along the (c) X-axis and (d) Y-axis. (e) Normalized intensity profile of the overlapping region integral along the (c) Y-axis. (f) Individual intensity of the interference fringes in the X-axis.

With the FRSI method, the electron beam can be measured even by the probe beam with a longer pulse duration because the region size of the interference fringes is not influenced by τ_{pro}. This is more obvious if the duration of the probe laser is increased from $100\,fs$ to $250\,fs$ with other parameters unchanged. For the measurement without self-interference, the intensity profile in the imaging plane of the CCD camera will be widened in the X direction due to the contribution of the probe beam duration, as shown in Fig. 5(a) and (d). Moreover, the width of the background intensity profile in the Y-axis in Fig. 5(c) is unchanged compared to the result in Fig. 4(c). The intensity distribution in the overlapping region also has a larger scale in the X-axis as presented in Fig. 5(b) and (e) compared with those in Fig. 4(b) and (e). However, the individual intensity profile of the interference fringes in Fig. 5(f) is as the same as the result in Fig. 4(f), which means that the measurement results are the same for a longer τ_{pro}. The region size of the interference region is independent of the probe laser duration.

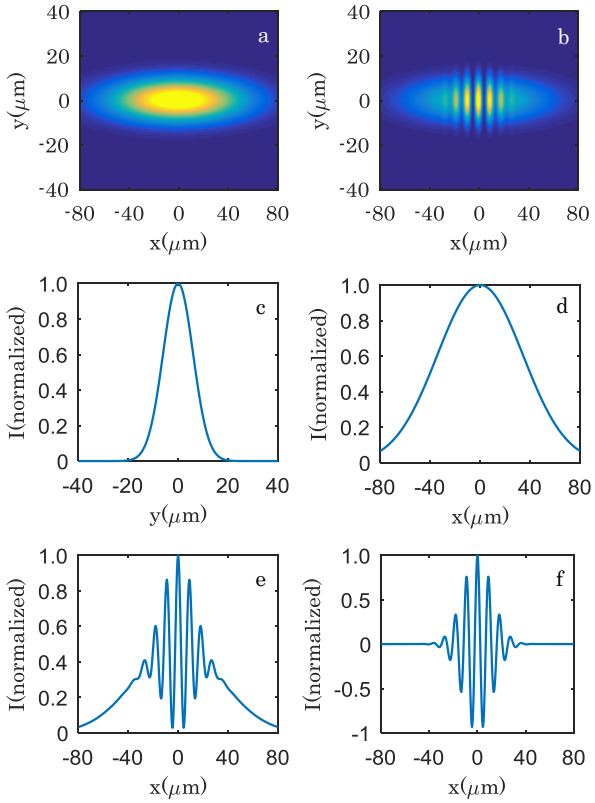

Figure 5. Intensity distributions of (a) L2 from Eq. (7) and (b) the interference fringes of L1 and L2 from Eq. (10) on the CCD imaging plane with $\tau_{pro} = 250fs$. Normalized intensity traces of the intensity distribution of L2 integral along the (c) X-axis and (d) Y-axis. (e) Normalized intensity profile of the overlapping region integral along the (c) Y-axis. (f) Individual intensity of the interference fringes in the X-axis.

5. Resolution of the FRSI method

In the FRSI method, the most important process is identifying the overlapping region from the background intensity. Since the overlapping region is characterized by the interference fringes, the measuring error is determined by the fringe interval η. If η is too large, the measurement of the region size is inaccurate. As η is inversely proportional to the propagation angle θ between L1 and L2 as $\eta = \lambda/\theta$, the measurement error is smaller at a larger θ as shown in Fig. 6(a). For $\theta = 5^o$, $\eta = 9.2\,\mu m$. However, η has to be larger than the pixel size Δs of the CCD camera in case the fringes is too close to identify, which limits the range of θ. The resolution of magnification system, which is $\eta \approx \lambda/2\theta N$, also affects the measurement of the region size. The corresponding error in determination of the electron beam duration is $\Delta\tau = \eta/c$. In the case in Fig. 4 and 5, the duration resolution $\Delta\tau \approx 1.5\,fs$. As plotted in Fig. 6(b), $\Delta\tau$ declines with the improvement of N and θ. For instance, the measurement error will be as small as $\sim 0.76fs$ if N=20 and $\theta = 5^o$. Moreover, the measurement inaccuracy of the electron beam duration limited by the CCD pixel size is determined by $\Delta L_{mag} = \pm\Delta s\sqrt{\left(L_{mag}^2 + 4r_{mag}^2\right)}/\sqrt{2}N^2L_{mag}$. In the case in Fig. 4 and 5, ΔL_{mag} is nearly $\pm 0.09\,\mu m$.

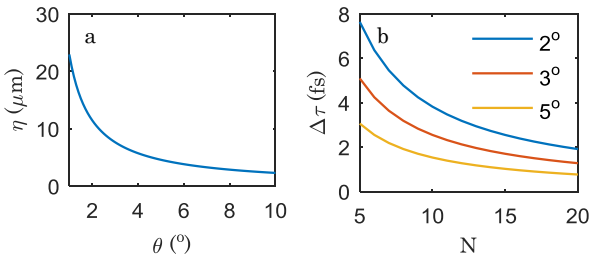

Figure 6. (a) Interference fringe interval vs. the incident angle assuming N=1. (b) Resolution of the measurement as function of N for different angle.

6. Conclusions

In this paper, we design and analyze the FRSI method for the electron beam duration in LWFAs, which is based on the faraday-rotation effect by the azimuthal magnetic field of the electron beam and Michelson interferometer. The polarization-rotated light is introduced into the interferometer to interfere with itself. Because the region size of the interference fringes is only related to the electron beam length and the radius of the magnetic region, the electron beam length measurement is independent of the pulse duration of the probe laser. And the measurement error of the beam duration could be reduced to less than $1fs$ with a higher magnification and larger incident angle.

References

1. F. S. Tsung, R. Narang, W. B. Mori, C. Joshi, R. A. Fonseca, and L. O. Silva, "Near-GeV-energy laser-wakefield acceleration of self-injected electrons in a centimeter-scale plasma channel," Physical Review Letters **93**(2004).
2. W. P. Leemans, B. Nagler, A. J. Gonsalves, C. Toth, K. Nakamura, C. G. R. Geddes, E. Esarey, C. B. Schroeder, and S. M. Hooker, "GeV electron beams from a centimetre-scale accelerator," Nature Physics **2,** 696 (2006).
3. S. P. D. Mangles, C. D. Murphy, Z. Najmudin, A. G. R. Thomas, J. L. Collier, A. E. Dangor, E. J. Divall, P. S. Foster, J. G. Gallacher, C. J. Hooker, D. A. Jaroszynski, A. J. Langley, W. B. Mori, P. A. Norreys, F. S. Tsung, R. Viskup, B. R. Walton, and K. Krushelnick, "Monoenergetic beams of relativistic electrons from intense laser-plasma interactions," Nature **431,** 535 (2004).
4. X. Wang, R. Zgadzaj, N. Fazel, Z. Li, S. A. Yi, X. Zhang, W. Henderson, Y. Y. Chang, R. Korzekwa, H. E. Tsai, C. H. Pai, H. Quevedo, G. Dyer, E. Gaul, M. Martinez, A. C. Bernstein, T. Borger, M. Spinks, M. Donovan, V. Khudik, G. Shvets, T. Ditmire, and M. C. Downer, "Quasi-monoenergetic laser-plasma acceleration of electrons to 2 GeV," Nat Commun **4**(2013).
5. W. P. Leemans, A. J. Gonsalves, H. S. Mao, K. Nakamura, C. Benedetti, C. B. Schroeder, C. Toth, J. Daniels, D. E. Mittelberger, S. S. Bulanov, J. L. Vay, C. G. R. Geddes, and E. Esarey, "Multi-GeV Electron Beams from Capillary-Discharge-Guided Subpetawatt Laser Pulses in the Self-Trapping Regime," Physical Review Letters **113**(2014).
6. X. L. Xu, C. H. Pai, C. J. Zhang, F. Li, Y. Wan, Y. P. Wu, J. F. Hua, W. Lu, W. An, P. Yu, C. Joshi, and W. B. Mori, "Nanoscale Electron Bunching in Laser-Triggered Ionization Injection in Plasma Accelerators," Physical Review Letters **117,** 034801 (2016).
7. M. Mirzaie, S. Li, M. Zeng, N. A. M. Hafz, M. Chen, G. Y. Li, Q. J. Zhu, H. Liao, T. Sokollik, F. Liu, Y. Y. Ma, L. M. Chen, Z. M. Sheng, and J. Zhang, "Demonstration of self-truncated

ionization injection for GeV electron beams," Scientific Reports **5**(2015).

8. W. T. Wang, W. T. Li, J. S. Liu, Z. J. Zhang, R. Qi, C. H. Yu, J. Q. Liu, M. Fang, Z. Y. Qin, C. Wang, Y. Xu, F. X. Wu, Y. X. Leng, R. X. Li, and Z. Z. Xu, "High-Brightness High-Energy Electron Beams from a Laser Wakefield Accelerator via Energy Chirp Control," Physical Review Letters **117,** 124801 (2016).
9. K. Nakajima, "Laser-driven electron beam and radiation sources for basic medical and industrial sciences," Proceedings of the Japan Academy Series B-Physical and Biological Sciences **91,** 223 (2015).
10. M. Geissler, J. Schreiber, and J. Meyer-ter-Vehn, "Bubble acceleration of electrons with few-cycle laser pulses," New Journal of Physics **8**(2006).
11. A. D. Debus, M. Bussmann, U. Schramm, R. Sauerbrey, C. D. Murphy, Z. Major, R. Hoerlein, L. Veisz, K. Schmid, J. Schreiber, K. Witte, S. P. Jamison, J. G. Gallacher, D. A. Jaroszynski, M. C. Kaluza, B. Hidding, S. Kiselev, R. Heathcote, P. S. Foster, D. Neely, E. J. Divall, C. J. Hooker, J. M. Smith, K. Ertel, A. J. Langley, P. Norreys, J. L. Collier, and S. Karsch, "Electron Bunch Length Measurements from Laser-Accelerated Electrons Using Single-Shot THz Time-Domain Interferometry," Physical Review Letters **104**(2010).
12. O. Lundh, J. Lim, C. Rechatin, L. Ammoura, A. Ben-Ismail, X. Davoine, G. Gallot, J. P. Goddet, E. Lefebvre, V. Malka, and J. Faure, "Few femtosecond, few kiloampere electron bunch produced by a laser-plasma accelerator," Nature Physics **7,** 219 (2011).
13. H. Kotaki, K. Kawase, Y. Hayashi, M. Mori, M. Kando, J. K. Koga, and S. V. Bulanovt, "Direct Observation of the Pulse Width of an Ultrashort Electron Beam," Journal of the Physical Society of Japan **84**(2015).
14. A. Buck, M. Nicolai, K. Schmid, C. M. S. Sears, A. Saevert, J. M. Mikhailova, F. Krausz, M. C. Kaluza, and L. Veisz, "Real-time observation of laser-driven electron acceleration," Nature Physics **7,** 543 (2011).
15. M. S. Bigelow, N. N. Lepeshkin, H. Shin, and R. W. Boyd, "Propagation of smooth and discontinuous pulses through materials with very large or very small group velocities," Journal of Physics-Condensed Matter **18,** 3117 (2006).
16. J. A. Stamper and B. H. Ripin, "FARADAY-ROTATION MEASUREMENTS OF MEGAGAUSS MAGNETIC-FIELDS IN LASER-PRODUCED PLASMAS," Physical Review Letters **34,** 138 (1975).